

# S3OD: TOWARDS GENERALIZABLE SALIENT OBJECT DETECTION WITH SYNTHETIC DATA

Orest Kupyn<sup>1</sup>, Hirokatsu Kataoka<sup>1,2</sup>, Christian Rupprecht<sup>1</sup>

<sup>1</sup>University of Oxford, VGG <sup>2</sup>AIST

<https://s3odproject.github.io>

## ABSTRACT

Salient object detection exemplifies data-bounded tasks where expensive pixel-precise annotations force separate model training for related subtasks like DIS and HR-SOD. We present a method that dramatically improves generalization through large-scale synthetic data generation and ambiguity-aware architecture. We introduce S3OD, a dataset of over 139,000 high-resolution images created through our multi-modal diffusion pipeline that extracts labels from diffusion and DINO-v3 features. The iterative generation framework prioritizes challenging categories based on model performance. We propose a streamlined multi-mask decoder that naturally handles the inherent ambiguity in salient object detection by predicting multiple valid interpretations. Models trained solely on synthetic data achieve 20-50% error reduction in cross-dataset generalization, while fine-tuned versions reach state-of-the-art performance across DIS and HR-SOD benchmarks.



Figure 1: *S3OD* Top: Our large scale synthetic dataset, consisting of diverse complex scenes and high quality samples. Bottom: Model Predictions. Our model trained on synthetic data generalizes well to real-world images, handling ambiguous scenes by predicting alternative hypothesis.

## 1 INTRODUCTION

Salient object detection (SOD) is a fundamental computer vision problem with applications spanning AR/VR Tian et al. (2022), robotics Chan & Riek (2020), 3D reconstruction Liu et al. (2021a), and image editing Goferman et al. (2011). Recently, two specialized subtasks have emerged: dichotomous image segmentation (DIS), focusing on highly accurate boundaries, and high-resolution SOD (HR-SOD) for 2K-8K resolution images, both presenting new generalization challenges. SOD exemplifies tasks fundamentally limited by labeled data availability. Creating diverse datasets requires extensive real-world scenarios, while pixel-precise annotation demands up to 10 hours per sample in DIS-5K Qin et al. (2022). Moreover, annotations often contain inherent ambiguities and inconsistencies across datasets, as annotators interpret scene saliency differently, a fundamental challenge that deterministic approaches fail to address. These constraints yield relatively small datasets Qin et al. (2022); Zeng et al. (2019) that cannot capture real-world complexity. Even large-scale datasets like SA-1B Ravi et al. (2024) struggle with the high-resolution pixel-perfect data that SOD demands Ke et al. (2023). Current approaches train separate models for DIS and HR-SOD due to small datasets and domain gaps, leading to task-specific overfitting rather than generalizable principles. Recent architectural innovations Yu et al. (2024); Zheng et al. (2024); Kim et al. (2022) yield incremental improvements but fail to address cross-domain generalization. The fundamental bottleneck remains data scarcity, not

---

model complexity, while models typically enforce deterministic predictions, ignoring fundamental ambiguity. Synthetic data offers an attractive solution, but existing approaches have critical limitations. Traditional pseudo-labeling setups are bounded by teacher capabilities and often use the same vision encoders, creating performance ceilings. Methods extending diffusion models to predict masks directly Wu et al. (2023a) suffer from consistency issues due to noisy diffusion features. In contrast, mask-conditioned generation Qian et al. (2024) struggles with diversity as obtaining large mask libraries and generating complex scenes remains challenging.

In this work, we aim to unify DIS and HR-SOD by addressing the two main limitations of prior work in these tasks. We refer to the unified task as high-fidelity salient segmentation. To this end, we introduce: 1) a multi-modal data generation pipeline that leverages the generative power of diffusion models, eliminating teacher bottlenecks, 2) an ambiguity-aware architecture handling multiple interpretations, and 3) an iterative generation framework adapting to model weaknesses. Our main contributions are:

**Multi-Modal Dataset Diffusion Pipeline:** Our diffusion pipeline simultaneously generates images and masks by extracting FLUX DiT features maps, concept attention maps, and DINO-v3 Siméoni et al. (2025) representations during the generation process. The generation pipeline harnesses rich spatial understanding encoded during generation alongside robust semantic features from self-supervised learning to decode high-quality masks. This ensures strong image-label alignment, enabling a flexible framework applicable to other dense prediction tasks.

**Iterative Generation Framework:** We introduce feedback-driven synthetic data generation that dynamically identifies model weaknesses, continuously adapting sampling distribution to prioritize challenging categories. Unlike traditional static methods, this iterative approach enables continuous improvement as datasets grow.

**Large-Scale Synthetic Dataset:** Using our pipeline, we generate 139,000+ high-resolution images with pixel-wise annotations, over  $2\times$  more than all existing SOD datasets combined. This enables up to 50% error reduction across benchmarks when evaluated for cross-dataset generalization. Models trained solely on synthetic data achieve remarkable cross-dataset generalization without real training data, while fine-tuned versions reach state-of-the-art performance across DIS and HR-SOD benchmarks.

**Ambiguity-Aware Architecture:** We directly address SOD’s inherent ambiguity through a multi-mask decoder allowing multiple valid interpretations while enabling a simpler architecture compared to current state-of-the-art methods. We employ DINO-v3 backbone, leveraging enhanced visual representations for improved generalization.

## 2 RELATED WORK

**Salient Object Detection:** SOD has evolved from handcrafted features Borji et al. (2015) to sophisticated high-resolution multi-view transformer architectures Yu et al. (2024). BASNet Qin et al. (2019) pioneered boundary-aware refinement with hybrid loss functions for precise object delineation, while subsequent work Zhao et al. (2019); Wei et al. (2020); Wu et al. (2019b); Feng et al. (2019) explored efficient edge-refinement strategies.  $U^2$ -Net Qin et al. (2020) developed nested UNet architecture to capture multi-scale contextual information. CPD Wu et al. (2019a) introduced cascaded decoders directly refining features with generated saliency maps. PFANet Zhang et al. (2018) and PAGENet Wang et al. (2019) leveraged pyramid attention networks to enhance segmentation quality. However, these approaches remain constrained by training dataset limitations and struggle with high-resolution inference scenarios. Recently, HR-SOD and DIS emerged as specialized subtasks focused on high-resolution accurate segmentation. IS-Net Qin et al. (2022) established the DIS baseline using intermediate supervision with feature-level and mask-level guidance. Newer approaches incorporated transformer backbones Liu et al. (2021b) to enhance feature extraction. InSPyReNet Kim et al. (2022) adapted image pyramid architecture for HR-SOD, while BiRefNet Zheng et al. (2024) introduced bilateral reference frameworks for capturing intricate details. MVANet Yu et al. (2024) recently proposed multi-view aggregation to detect finer details while improving efficiency. Nevertheless, these methods produce single deterministic outputs and remain constrained by limited training data. Our approach addresses both limitations while simplifying architecture.

**Synthetic Data Generation:** Diffusion models have transformed data generation by enabling high-quality, diverse synthetic datasets. Recent work Shipard et al. (2023); Sarıyıldız et al. (2023); Tian

et al. (2023); Azizi et al. (2023); Fan et al. (2024) improved classification model performance through synthetic data generation with latent diffusion models Rombach et al. (2022), though limited to image classification. DiffuMask Wu et al. (2023b), Attn2mask Yoshihashi et al. (2024), and DatasetDM Wu et al. (2023a) utilize diffusion models to generate synthetic images with annotations for segmentation tasks. However, DatasetDM’s attention-based extraction produces noisy, incomplete masks lacking precise boundaries and struggling with complex multi-object scenes. OVDiff Karazija et al. (2024) synthesises support image sets for arbitrary textual categories, while Instance Augmentation Kupyn & Rupprecht (2024) provides augmentation frameworks but only slightly expands original distributions. VGGHeads Kupyn et al. (2024) demonstrated synthetic data’s impact on generalization for 3D head modeling but remains bounded by external teacher models. For SOD specifically, SODGAN Wu et al. (2022) employs GANs but struggles with complex scenes due to limited training data variability. MaskFactory Qian et al. (2024) conditions image generation on edited masks but is limited to only creating slight variations of the train set. Unlike these approaches relying on noisy attention extraction, mask conditioning, or external teacher models, our method extracts supervision from multiple complementary sources within the generative process itself. By combining DINO-v3 Siméoni et al. (2025) visual features, diffusion transformer activations, and concept attention maps Helbling et al. (2025), we achieve robust supervision with strong image-mask alignment while eliminating performance bottlenecks.

### 3 MODEL

Most recent salient object detection methods focus on improving performance through complex architectural components such as multi-view feature fusion Yu et al. (2024) or iterative refinement modules Zheng et al. (2024). In contrast, we propose a lightweight architecture that primarily addresses SOD ambiguity through a multi-mask decoder while significantly simplifying other components.

#### 3.1 MODEL ARCHITECTURE

We build our model upon the Dense Prediction Transformer (DPT) Ranftl et al. (2021) architecture, which processes input images through transformer Vaswani et al. (2017) stages followed by multi-scale feature reassembly. DPT transforms input into patch token sequences, processes them through transformer layers, then reconstructs multi-scale image-like representations. These features are progressively fused and upsampled through residual convolutional blocks He et al. (2016) to produce final predictions. We adopt this efficient hierarchical design as our backbone. We initialize the DPT encoder with DINO-v3 weights to improve generalization, leveraging visual representations from large-scale self-supervised training. The full architecture is shown in Figure 2.

We formulate the problem as function  $f : \mathcal{I} \rightarrow \mathcal{M}$  mapping from images  $\mathcal{I} \subset \mathbb{R}^{H \times W \times 3}$  to binary masks  $\mathcal{M} = \{0, 1\}^{H \times W}$  of spatial resolution  $H \times W$ . Many training annotations contain ambiguity: multiple objects may be present with unclear saliency interpretation. Single-output models tend to average all possible predictions, resulting in low-confidence regions.

To address this, we design the final mask prediction head to output multiple masks  $(m_1, \dots, m_N)$ . Predicted masks are soft  $m_i \in (0, 1)^{H \times W}$  to model pixel-wise confidence. For each training image  $I \in \mathcal{I}$ , only one ground truth annotation  $y \in \mathcal{M}$  is available. Inspired by multiple-choice learning Guzman-Rivera et al. (2012), during training, the main loss applies to the best prediction  $i^* = \arg \min_i \text{IoU}(m_i, y)$ , chosen via IoU score between predicted and ground truth masks.

To prevent unused branches from degrading, we employ relaxed assignment Rupprecht et al. (2017) where loss is computed across all branches with decaying weight:  $\mathcal{L} = \mathcal{L}_{i^*} + \lambda e^{-\gamma t} \sum_i^N \mathcal{L}_i$ , where  $\lambda$  controls initial auxiliary branch weight,  $\gamma$  is decay rate,  $t$  is current epoch. Individual losses  $\mathcal{L}_i = \mathcal{L}(m_i, y)$  are described next. For test-time selection, the model estimates IoU scores  $(s_1, \dots, s_N)$  for every prediction. This is supervised by actual IoU scores between prediction and ground truth during training and this estimate is used to select the highest-scoring mask during testing.

#### 3.2 OBJECTIVE FUNCTION

Following standard semantic segmentation practice, we employ a multi-component loss combining pixel-wise and region-wise supervision. The total loss  $\mathcal{L}$  consists of two main components: **Focal Loss** Lin et al. (2017)  $\mathcal{L}_{\text{focal}}$  for handling class imbalance and **IoU Loss**  $\mathcal{L}_{\text{IoU}}$  for region-level accuracy.

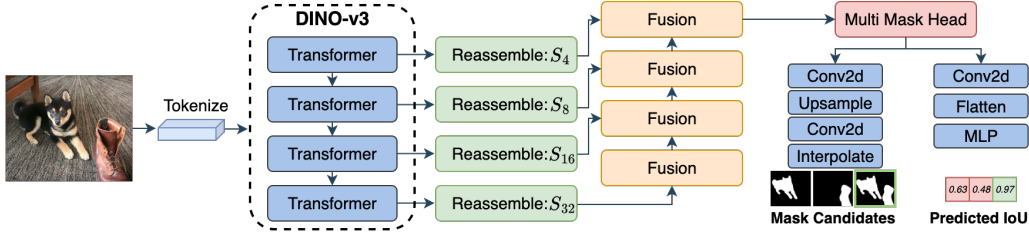


Figure 2: **S3OD Architecture.** Model extends DPT Ranftl et al. (2021) to predict multiple mask candidates and a vector of IoUs with the ground truth, employing DINO-v3 as the backbone. During training, the loss is propagated through the branch with the highest predicted IoU.

**Focal Loss.** To address foreground-background imbalance, we implement focal loss, widely used in dense prediction:

$$\mathcal{L}_{\text{focal}}(m_i) = - \sum_{p=1}^{H \times W} (1 - m_i(p))^\tau y(p) \log(m_i(p))$$

where  $p$  iterates over pixels indexing predicted mask  $m_i(p)$  and ground truth  $y(p)$ , and  $\tau = 2$  is the focusing parameter.

**IoU Loss.** To capture region-level accuracy, we incorporate IoU loss measuring overlap between predicted and ground truth masks:

$$\mathcal{L}_{\text{IoU}}(m_i) = 1 - \frac{\sum_{p=1}^{H \times W} m_i(p)y(p)}{\sum_{p=1}^{H \times W} (m_i(p) + y(p) - m_i(p)y(p))}$$

The overall mask loss combines both components:

$$\mathcal{L}_{\text{mask}}(m_i) = \lambda_{\text{mask}} \mathcal{L}_{\text{focal}}(m_i) + \mathcal{L}_{\text{IoU}}(m_i, y)$$

where  $\lambda_{\text{mask}} = 10$  balances the losses.

**IoU Score Loss.** To enable optimal mask selection at inference, we supervise predicted IoU scores  $s_i$  using mean squared error between predicted and actual IoU values:

$$\mathcal{L}_{\text{score}}(s_i) = (s_i - \text{IoU}(m_i, y))^2$$

Finally, the overall training objective comprises the mask loss of best prediction, score loss for all predictions, and a decaying regularizer across all predicted masks:

$$\mathcal{L}_{\text{mask}}(m_{i^*}) + \sum_{i=1}^N \lambda_{\text{score}} \mathcal{L}_{\text{score}}(s_i) + \lambda_{\text{reg}} e^{-\gamma t} \mathcal{L}_{\text{mask}}(m_i)$$

where  $\lambda_{\text{score}} = 0.05$ ,  $\lambda_{\text{reg}} = 0.1$  weigh the losses,  $\gamma = 0.2$  is decay rate,  $t$  is current epoch, and  $N$  is the number of prediction branches.

## 4 DATASET

Unlike other dense prediction tasks, scaling SOD datasets faces unique challenges that cannot be solved by simply leveraging existing collections like LAION Schuhmann et al. (2022). SOD requires samples with distinct foreground objects, and annotation demands significant expertise and meticulous attention to detail, particularly for high-resolution images with precise boundary requirements. These constraints make traditional manual dataset curation both impractical and cost-inefficient. Our goal is to generate large-scale synthetic data that accurately reflects real-world distributions.

### 4.1 MULTI-MODAL DATASET DIFFUSION

Large-scale diffusion transformers like FLUX Labs (2023) with 12B parameters encode rich semantic and spatial representation during the generation process. Rather than ignoring these latent representations and relying on teacher models that predict masks directly from generated images, we extend the diffusion model to output masks by combining multiple complementary modalities. Our approach extracts latent feature maps that encode spatial layout understanding, concept attention maps that

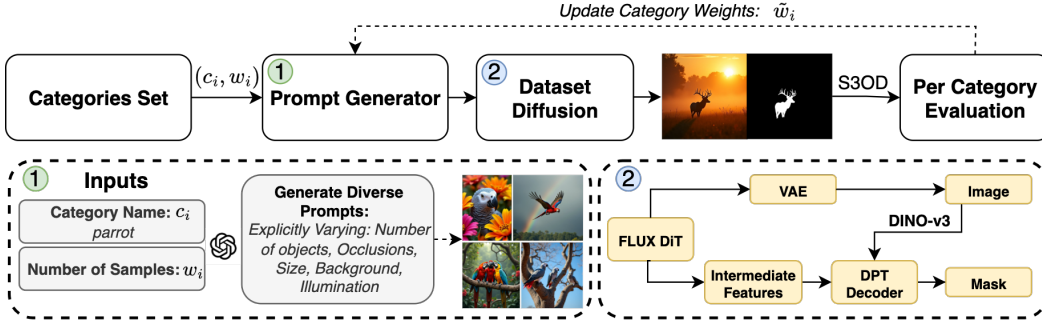


Figure 3: **Iterative Generation Pipeline.** The LLM Achiam et al. (2023) generates a library of diverse prompts for a large set of object categories. These prompts guide a diffusion model to generate synthetic images with corresponding masks. The resulting dataset trains SOD model, which undergoes category-wise evaluation. Performance feedback from a trained SOD model dynamically adjusts category weights  $\tilde{w}_i$ , prioritizing challenging cases in subsequent iterations.

provide interpretable semantic localization, and DINO-v3 features from decoded images that capture fine-grained visual semantics. This multi-modal supervision mitigates data scarcity while ensuring alignment between generated images and corresponding masks.

**DiT Feature Maps.** FLUX DiT employs a hybrid architecture with 19 dual-stream transformer blocks (processing text and image tokens separately) and 38 single-stream blocks (operating on concatenated sequences). We extract feature maps from four single-stream transformer blocks at layers  $\{4, 16, 27, 36\}$ , capturing multi-scale spatial representations across generation stages. Each block outputs features  $\mathbb{R}^{B \times (L_T + L_I) \times 3072}$  where  $L_T = 512$ . We extract only image tokens  $\mathbb{R}^{B \times L_I \times 3072}$  and project to 768 dimensions via learned projections. These features encode the model’s internal spatial reasoning used during synthesis.

**Concept Attention Maps.** Common dataset generation methods Wu et al. (2023a) extract mean attention maps across all text tokens, producing semantically ambiguous supervision. Instead, we use a static set of concepts to obtain interpretable, consistent maps. Following the concept attention framework Helbling et al. (2025), for each generated image, we compute attention maps between image patches and specific concept tokens. For concept token  $c$  and image patch  $x$ , we compute:

$$A_{concept}(x, y) = \text{softmax}(o_x \cdot o_c^T)$$

where  $o_x$  and  $o_c$  are attention output vectors from the multi-modal transformer layers. For each sample, we extract two concept attention maps using the primary object category (e.g., "dog") and "background" tokens, yielding interpretable maps  $\{A_{object}, A_{background}\}$  that consistently encode object location and background regions.

**DINO-v3 Visual Features.** We extract semantic visual features from generated images using DINO-v3 (ViT-L), providing rich object-level representations that capture fine-grained visual semantics through self-supervised learning on diverse real-world imagery.

The three modalities are fused through a dedicated module that projects each to a common 256-dimensional space via separate convolutional branches with batch normalization. FLUX features and concept maps are upsampled to match DINO-v3 resolution using bilinear interpolation. The projected features are concatenated channel-wise and processed through a two-stage convolutional network ( $3 \times 3$  followed by  $1 \times 1$  convolution), with the result residually combined with the original DINO-v3 features to produce unified multi-modal representations.

## 4.2 ITERATIVE DATA SYNTHESIS

To incorporate a feedback mechanism into the data generation, we introduce an iterative process that adjusts generation parameters based on the downstream model’s performance for subsequent rounds. After training the model on synthetic data  $\mathcal{D}^{(r)}$ , we evaluate its performance on a held-out test set for each category  $c_i$ . For each image  $I_j$ , we compute a score  $\kappa(I_j)$ , which is the average IoU score across various image transformations (flipping, etc.).  $\kappa(I_j)$  is high if the prediction is good across all augmentations. We then compute a mean category score  $\bar{\kappa}_i$  by averaging these scores across all

Table 1: **SOD Datasets Statistics:** S3OD dataset is order of magnitudes larger than existing datasets and contain a wide variety of scenes and objects.

Metric	DUTS	ECSSD	HKU-IS	DUT-OMRON	UHRSD	HRSOD	DIS-5K	S3OD (ours)
# of Images	15,570	1,000	4,447	5,168	5,920	2,010	5,000	139,981
# of Unique Objects	1152	310	551	749	948	381	758	1676



Figure 4: **S3OD Dataset:** The dataset consists of diverse object categories and complex scenes that closely reflect real-world environments, featuring various lighting conditions, spatial compositions, and object interactions. All samples are generated with multi-modal dataset diffusion.

images in category  $c_i$ . The category weights  $w_i^{(r+1)}$  for the next iteration are updated proportionally to the inverse of these scores, ensuring categories with lower performance receive more samples in subsequent generations. Specifically, we map the category scores through a non-linear scaling function:  $w_i^{(r+1)} = w_{\min} + w_{\text{new}} e^{-\alpha(\bar{\kappa}_i - \beta)}$ , where  $\alpha = 8$  and  $\beta = 0.5$  control the strength of the performance-based skew,  $w_{\min} = \frac{1}{|C|}$  is a minimum weight per class, and  $w_{\text{new}} = \frac{4}{|C|}$  is the maximal possible over-weighting. This scales up weights for categories with scores below a certain threshold while maintaining a minimum weight for well-performing categories. This adaptive sampling strategy ensures that the synthetic data generation process continuously evolves, producing examples that maximize model improvement. The pipeline is visualized in Figure 3.

### 4.3 MULTI-STAGE QUALITY FILTERING

While synthetic data generation offers scalability, it inevitably produces imperfect samples that can degrade training quality. To ensure high dataset quality, we implement a comprehensive multi-stage filtering pipeline that addresses standard failure modes in synthetic data generation.

**Consistency Filtering.** We evaluate prediction consistency using a separate large model trained without FLUX features. For each sample, we compute IoU between the original prediction and horizontally-flipped prediction, filtering samples below  $\tau = 0.8$  consistency threshold. Low consistency scores often indicate overly ambiguous samples where even robust models struggle to maintain coherent predictions, suggesting fundamental issues with the generated image-mask pairs.

**Mask Quality Assessment.** We employ a Gemma-3 VLM Team et al. (2025) to evaluate mask quality, identifying severe artifacts such as fragmentation, salt-and-pepper noise, or swiss-cheese effects that commonly occur in synthetic mask generation. Only masks with cohesive white regions ( $\leq 5$  main components) pass this stage, ensuring clean supervision signals for model training.

**Semantic Validation.** In a second pass, the Gemma VLM evaluates semantic correctness by analyzing the original image alongside the mask overlay. This stage ensures both the presence of clear salient objects and adequate mask coverage ( $> 70\%$  of the main object), filtering out samples where the multi-modal supervision fails to capture the intended semantic content.

This multi-stage approach removes 6.8% of generated samples, significantly improving dataset quality while maintaining scale advantages over manual annotation.

### 4.4 IMPLEMENTATION DETAILS

We generate 139,981 high-resolution data samples in three rounds ( $R = 3$ ) which is **131%** more than 11 most common academic benchmarks combined. The initial round produces 100 images per category, followed by a second and third round that generate an additional 50,000 images, emphasizing challenging categories. During processing, 6.8% of the samples are filtered out. The images are generated with a FLUX model with inference steps set to 25. For each image, the aspect ratio is randomly sampled from a fixed set of common image resolutions, further expanding dataset variety. All student models are trained with the ViT-B Dosovitskiy et al. (2020) backbone. Model training on S3OD dataset takes 2 days on 8 H200 GPUs.

Table 2: **Cross-Dataset Generalization:** S3OD trained on synthetic data only demonstrates superior generalization across all datasets comparing to other methods trained on subtasks datasets. SOD datasets stand for (HRSOD-TR Zeng et al. (2019), UHRSD-TR Xie et al. (2022) and DUTS-TR Wang et al. (2017)). **Best** and **second best** results highlighted.

Method	Data	DIS-1				DIS-2				DIS-3				DIS-4				Overall			
		$F_m \uparrow$	$S_\alpha \uparrow$	$E_M^\Phi \uparrow$	MAE $\downarrow$	$F_m \uparrow$	$S_\alpha \uparrow$	$E_M^\Phi \uparrow$	MAE $\downarrow$	$F_m \uparrow$	$S_\alpha \uparrow$	$E_M^\Phi \uparrow$	MAE $\downarrow$	$F_m \uparrow$	$S_\alpha \uparrow$	$E_M^\Phi \uparrow$	MAE $\downarrow$	$F_m \uparrow$	$S_\alpha \uparrow$	$E_M^\Phi \uparrow$	MAE $\downarrow$
InSpyreNet	DUTS	.786	.822	.857	.064	.828	.845	.877	.057	.839	.848	.883	.059	.789	.806	.838	.082	.811	.830	.864	.065
BiRefNet	SOD	.812	.841	.863	.049	.844	.855	.877	.050	.855	.856	.881	.053	.790	.803	.824	.081	.825	.839	.861	.058
S3OD	SOD	.850	.885	.902	.046	.880	.870	.914	.043	.888	.875	.928	.040	.833	.823	.881	.069	.863	.856	.906	.049
S3OD	S3OD	.865	.884	.917	.034	.896	.898	.933	.032	.901	.895	.938	.033	.861	.857	.913	.054	.881	.884	.925	.039

Method	Data	DAVIS-S				HRSOD-TE				UHRSD-TE				DUTS-TE				DUT-OMRON			
		$F_m \uparrow$	$S_\alpha \uparrow$	$E_M^\Phi \uparrow$	MAE $\downarrow$	$F_m \uparrow$	$S_\alpha \uparrow$	$E_M^\Phi \uparrow$	MAE $\downarrow$	$F_m \uparrow$	$S_\alpha \uparrow$	$E_M^\Phi \uparrow$	MAE $\downarrow$	$F_m \uparrow$	$S_\alpha \uparrow$	$E_M^\Phi \uparrow$	MAE $\downarrow$	$F_m \uparrow$	$S_\alpha \uparrow$	$E_M^\Phi \uparrow$	MAE $\downarrow$
InSpyreNet	DIS	.921	.937	.966	.015	.891	.912	.923	.038	.914	.922	.932	.033	.845	.880	.895	.046	.713	.801	.812	.071
BiRefNet	DIS	.919	.936	.961	.014	.887	.915	.926	.031	.922	.924	.937	.032	.860	.886	.910	.036	.744	.819	.835	.054
MVANet	DIS	.907	.929	.959	.016	.902	.919	.930	.033	.922	.926	.941	.032	.852	.877	.893	.042	.711	.792	.838	.072
S3OD	DIS	.951	.950	.973	.010	.923	.913	.932	.030	.946	.927	.947	.029	.902	.901	.926	.035	.808	.830	.858	.061
S3OD	S3OD	.970	.967	.988	.005	.954	.955	.972	.016	.954	.944	.961	.023	.937	.938	.962	.020	.860	.887	.911	.040

## 5 EXPERIMENTAL EVALUATION

We extensively evaluate the dataset and model generalization capabilities and performance on various benchmarks.

### 5.1 EVALUATION PROTOCOL

The performance of the salient object detection models is evaluated on six datasets of two domains. For dichotomous image segmentation (DIS), we use DIS-5K Qin et al. (2022), containing 5,470 high-resolution images with extremely fine-grained labels of camouflaged, salient, and meticulous objects in varied backgrounds. For Salient Object Detection (HR-SOD), we evaluate on three high-resolution benchmarks: UHRSD Xie et al. (2022) (5,920 images at 4K-8K resolution), HRSOD-TE Zeng et al. (2019) (400 test images with shortest edge >1200 pixels), and DAVIS-S (92 images from DAVIS Pont-Tuset et al. (2017) video segmentation dataset). We also include two low-resolution benchmarks: DUT-OMRON Yang et al. (2013) (5,168 images with complex backgrounds) and DUTS-TE Wang et al. (2017) (5,019 test images from the largest available SOD dataset). All datasets feature pixel-wise ground truth annotations for quantitative evaluation.

**Metrics.** We measure the performance of the model on each dataset using widely adopted metrics: maximum F-measure ( $F_{1max}$ ) Achanta et al. (2009), Mean Average Error (MAE) Perazzi et al. (2012), structure measure ( $S_\alpha$ ) Fan et al. (2017) and enhanced alignment measure ( $E_M^\Phi$ ) Fan et al. (2018). The F-measure ( $F_\beta$ ) provides a balanced evaluation between precision and recall, computed with  $\beta^2 = 0.3$  to emphasize precision. MAE calculates the average absolute difference between predicted and ground truth masks, where lower values indicate better performance. The structure measure  $S_\alpha$  evaluates preservation of object-aware ( $S_o$ ) and region-aware ( $S_r$ ) structural similarities, computed as  $S_m = \alpha * S_o + (1 - \alpha) * S_r$  with  $\alpha = 0.5$ . The enhanced alignment measure  $E_M^\Phi$  combines local and global similarity information, jointly capturing image-level statistics and local pixel matching information.

### 5.2 CROSS-DATASET GENERALIZATION

We argue that the most important aspect of modern salient object segmentation models should be generalizing to new image distributions. We evaluate the cross-task generalization by training the model on DIS-5K Qin et al. (2022) dataset and evaluating on SOD benchmarks and vice versa. The robust generalizable method is expected to perform well on all benchmark datasets, given that all focus on the same high-level problem. The results are presented in Table 2. S3OD trained on a combination of SOD datasets achieves superior generalization comparing to BiRefNet Zheng et al. (2024) or InSpyreNet Kim et al. (2022).

Remarkably, even training solely on synthetic data enables the method to achieve state-of-the-art generalization, reducing the MAE compared to the model trained on DIS-5K by **50.0%**, **46.7%**, **20.7%**, **42.9%**, and **34.4%**. The models trained on DIS-5K only (3000 images) and evaluated on SOD benchmarks all achieve comparable results, proving an importance of the data scale and and

Table 3: Quantitative comparison on DIS5K and SOD benchmarks. Best results highlighted in **bold**. The S3OD \* are the metrics computed with the best match over three predicted masks.

Method	DIS-1				DIS-2				DIS-3				DIS-4				Overall			
	$F_m \uparrow$	$S_\alpha \uparrow$	$E_M^\Phi \uparrow$	MAE $\downarrow$	$F_m \uparrow$	$S_\alpha \uparrow$	$E_M^\Phi \uparrow$	MAE $\downarrow$	$F_m \uparrow$	$S_\alpha \uparrow$	$E_M^\Phi \uparrow$	MAE $\downarrow$	$F_m \uparrow$	$S_\alpha \uparrow$	$E_M^\Phi \uparrow$	MAE $\downarrow$	$F_m \uparrow$	$S_\alpha \uparrow$	$E_M^\Phi \uparrow$	MAE $\downarrow$
SAM-HQ	<b>.897</b>	<b>.907</b>	<b>.943</b>	<b>.019</b>	.889	.883	.928	.029	.851	.851	.897	.045	.763	.799	.843	.088	.850	.860	.903	.045
InSpyreNet	.845	.873	.874	.043	.894	.905	.916	.036	.919	.918	.940	.034	.905	<b>.905</b>	.936	.042	.891	.900	.917	.039
BiRefNet	.860	.885	.911	.037	.894	.900	.930	.036	.925	.919	.955	.028	.904	.900	.939	.039	.896	.901	.934	.035
MVANet	.862	.880	.906	.039	.909	.912	.942	.032	.924	.918	.954	.030	.907	<b>.905</b>	.946	.039	.900	.904	.937	.035
S3OD	.892	.902	.932	.031	<b>.923</b>	<b>.921</b>	<b>.953</b>	<b>.026</b>	<b>.930</b>	<b>.920</b>	<b>.960</b>	<b>.025</b>	<b>.909</b>	.902	<b>.954</b>	<b>.034</b>	<b>.914</b>	<b>.911</b>	<b>.950</b>	<b>.029</b>
S3OD *	.916	.924	.960	.018	.941	.936	.973	.016	.941	.931	.975	.018	.914	.907	.967	.027	.928	.924	.969	.020

Method	DAVIS-S				HRSOD-TE				UHRSD-TE				DUTS-TE				DUT-OMRON			
	$F_m \uparrow$	$S_\alpha \uparrow$	$E_M^\Phi \uparrow$	MAE $\downarrow$	$F_m \uparrow$	$S_\alpha \uparrow$	$E_M^\Phi \uparrow$	MAE $\downarrow$	$F_m \uparrow$	$S_\alpha \uparrow$	$E_M^\Phi \uparrow$	MAE $\downarrow$	$F_m \uparrow$	$S_\alpha \uparrow$	$E_M^\Phi \uparrow$	MAE $\downarrow$	$F_m \uparrow$	$S_\alpha \uparrow$	$E_M^\Phi \uparrow$	MAE $\downarrow$
InSpyreNet	.977	.973	.987	.007	.956	.956	.962	.018	.957	.953	.965	.020	.932	.936	.956	.024	.823	.872	.906	.046
BiRefNet	<b>.979</b>	<b>.975</b>	.989	.006	<b>.963</b>	.957	.973	.016	.963	<b>.957</b>	<b>.969</b>	<b>.016</b>	.943	.944	.962	.018	.839	.882	.896	.038
S3OD	<b>.979</b>	.974	<b>.993</b>	<b>.004</b>	<b>.963</b>	<b>.961</b>	<b>.978</b>	<b>.013</b>	<b>.964</b>	.952	<b>.969</b>	.018	<b>.954</b>	<b>.949</b>	<b>.972</b>	<b>.015</b>	<b>.879</b>	<b>.898</b>	<b>.924</b>	<b>.032</b>
S3OD *	.982	.977	.993	.004	.979	.973	.991	.005	.977	.966	.985	.008	.963	.959	.987	.008	.907	.919	.953	.023

impact of overfitting to the subtask specifics. Still, S3OD trained on synthetic data demonstrates strong generalization across all benchmarks.

### 5.3 STATE-OF-THE-ART COMPARISON

Prior work does not evaluate cross-task generalization and trains task/benchmark-specific models. While we argue that the evaluation above is the way forward for salient object segmentation, we also evaluate in the historically used setting. We finetune the model trained on our S3OD dataset on both the DIS-5K Qin et al. (2022) and a combination of SOD datasets (HR-SOD Zeng et al. (2019), UHRSD Xie et al. (2022), DUTS-TR Wang et al. (2017)). We report the results in Table 3. S3OD significantly outperforms all the other methods on DIS-5K benchmarks achieving a new state-of-the-art and reducing the error rate by **14.0%**, **7.3%**, **20.6%** and **17.1%**.

However, the salient object detection benchmarks have become highly saturated. S3OD achieves superior results on HRSOD-TE Zeng et al. (2019), DUTS-TE Wang et al. (2017), and DUT-OMRON Yang et al. (2013), even though all models are trained on the first two datasets. The evaluation on the DUT-OMRON benchmark serves as the strongest generalization test as none of the models were trained or fine-tuned on it, and the benchmark consists of 5,168 samples. S3OD achieve **24.8%**, **13.6%**, **26.9%** and **15.8%** reduction in error rate compared to BiRefNet. Notably, on UHRSD Xie et al. (2022), which is the largest HR-SOD train dataset and DAVIS-S, which contains only 92 images, all large models with transformer backbones achieve comparable results. This is another indicator of benchmark saturation and supports our choice of cross-task generalization evaluation. The variant S3OD \* computes the metrics with the best match of the three masks with the ground truth mask. This oracle evaluation uses ground truth information and cannot be compared to other methods. However, it demonstrates the inherent ambiguity in the data annotations and/or the task. This confirms that our choice of ambiguity-aware modelling will be highly useful in practical applications.

### 5.4 SYNTHETIC DATA EVALUATION

We also evaluate our data generation mechanism compared to other data synthesis methods. We measure the impact of synthetic data on performance and generalization, evaluating S3OD and other synthetic data generation methods Wu et al. (2023a); Qian et al. (2024). MaskFactory Qian et al. (2024) augments the DIS-5K Qin et al. (2022) dataset with both rigid and non-rigid transforms and generates a new set of images conditioned on augmented masks. To ensure fair comparison, we train our model on DIS-5K and a mix of DIS-5K and three synthetic datasets. Since the other two synthetic datasets contain only 10,000 train images, we also subsample a subset from S3OD of the same size from the 2nd iteration of data generation. We evaluate the model both on DIS and SOD benchmarks. The results are presented in Table 4.

**Results.** Interestingly, S3OD achieves comparable performance to MaskFactory Qian et al. (2024) on the DIS-5K test set, even though it was not fine-tuned for categories and types of object in this benchmark, despite MaskFactory utilising the DIS-5K train set to generate augmented masks. On other four SOD benchmarks S3OD demonstrates significantly stronger generalization and performance, comparing to both original train dataset and other synthetic data generation methods, proving the diversity and versatility of our data generation method.

Table 4: **Synthetic Data Generation Evaluation:** S3OD model is trained on a combination of DIS-5K and three synthetic datasets. Training with S3OD dataset significantly improves generalization.

Training Data	DIS (1-4)				HRSOD-TE				UHRSD-TE				DUTS-TE				DUT-OMRON			
	$F_m \uparrow$	$S_\alpha \uparrow$	$E_M^\Phi \uparrow$	MAE $\downarrow$	$F_m \uparrow$	$S_\alpha \uparrow$	$E_M^\Phi \uparrow$	MAE $\downarrow$	$F_m \uparrow$	$S_\alpha \uparrow$	$E_M^\Phi \uparrow$	MAE $\downarrow$	$F_m \uparrow$	$S_\alpha \uparrow$	$E_M^\Phi \uparrow$	MAE $\downarrow$	$F_m \uparrow$	$S_\alpha \uparrow$	$E_M^\Phi \uparrow$	MAE $\downarrow$
DIS	.910	.897	.943	.032	.923	.913	.932	.032	.946	.927	.947	.030	.902	.901	.925	.036	.808	.830	.858	.061
DIS + MaskFactory	.912	.904	<b>.950</b>	<b>.030</b>	.910	.916	.936	.031	.937	.926	.947	.030	.886	.898	.924	.038	.774	.812	.842	.071
DIS + DatasetDM	.898	.889	.939	.036	.899	.896	.911	.041	.932	.914	.934	.037	.872	.877	.900	.048	.770	.795	.818	.080
DIS + S3OD	.908	<b>.905</b>	.945	<b>.030</b>	<b>.944</b>	<b>.946</b>	<b>.963</b>	<b>.020</b>	<b>.950</b>	<b>.940</b>	<b>.958</b>	<b>.024</b>	<b>.924</b>	<b>.928</b>	<b>.951</b>	<b>.025</b>	<b>.842</b>	<b>.871</b>	<b>.899</b>	<b>.048</b>

Table 5: **Iterative Data Generation Ablation:** Progressively generating hard samples improves model performance and generalization across all datasets.

Training Data	DIS (1-4)				HRSOD-TE				DUTS-TE				DUT-OMRON			
	$F_m \uparrow$	$S_\alpha \uparrow$	$E_M^\Phi \uparrow$	MAE $\downarrow$	$F_m \uparrow$	$S_\alpha \uparrow$	$E_M^\Phi \uparrow$	MAE $\downarrow$	$F_m \uparrow$	$S_\alpha \uparrow$	$E_M^\Phi \uparrow$	MAE $\downarrow$	$F_m \uparrow$	$S_\alpha \uparrow$	$E_M^\Phi \uparrow$	MAE $\downarrow$
S3OD Single Round	.879	.883	.916	.041	.951	.953	.969	.018	.933	.935	.959	<b>.020</b>	.855	.881	.907	.042
S3OD (2 rounds)	.880	<b>.884</b>	.918	.040	.953	.954	.971	.017	.935	<b>.939</b>	.961	<b>.020</b>	.859	.885	.908	<b>.040</b>
S3OD (3 rounds)	<b>.881</b>	<b>.884</b>	<b>.925</b>	<b>.039</b>	<b>.954</b>	<b>.955</b>	<b>.972</b>	<b>.016</b>	<b>.937</b>	.938	<b>.962</b>	<b>.020</b>	<b>.860</b>	<b>.887</b>	<b>.911</b>	<b>.040</b>

## 5.5 ABLATION STUDY

Table 6: **Data Diffusion Model Ablation:** Combining all three modalities achieves optimal performance across benchmarks.

DINO-v3	DiT Maps	Concept Maps	DIS (1-4)				HRSOD-TE				UHRSD-TE				DUTS-TE				DUT-OMRON			
			$F_m \uparrow$	$S_\alpha \uparrow$	$E_M^\Phi \uparrow$	MAE $\downarrow$	$F_m \uparrow$	$S_\alpha \uparrow$	$E_M^\Phi \uparrow$	MAE $\downarrow$	$F_m \uparrow$	$S_\alpha \uparrow$	$E_M^\Phi \uparrow$	MAE $\downarrow$	$F_m \uparrow$	$S_\alpha \uparrow$	$E_M^\Phi \uparrow$	MAE $\downarrow$	$F_m \uparrow$	$S_\alpha \uparrow$	$E_M^\Phi \uparrow$	MAE $\downarrow$
×	✓	✓	.710	.743	.783	.091	.733	.784	.789	.097	.865	.868	.890	.054	.773	.805	.840	.070	.681	.733	.772	.095
✓	×	✓	.913	.909	.949	.029	.959	.958	.974	.014	.965	.953	<b>.971</b>	.017	<b>.950</b>	.945	.968	.017	.870	.887	.911	.036
✓	✓	×	.914	.906	.944	.030	.961	.957	.972	.014	.965	.952	<b>.971</b>	.016	.949	.943	.966	.017	.871	.889	.915	.036
✓	✓	✓	<b>.917</b>	<b>.913</b>	<b>.951</b>	<b>.028</b>	<b>.962</b>	<b>.961</b>	<b>.976</b>	<b>.012</b>	<b>.966</b>	<b>.953</b>	<b>.971</b>	<b>.016</b>	.948	<b>.944</b>	<b>.969</b>	<b>.016</b>	<b>.873</b>	<b>.891</b>	<b>.918</b>	<b>.034</b>

We evaluate our multi-modal data diffusion approach and architectural components. Table 6 shows individual feature types are insufficient: diffusion features alone cannot decode high-resolution masks, while DINO-v3, despite strong performance, can suffer from train-test distribution gaps when applied to generated images. The combination of all three modalities achieves optimal performance across benchmarks, with diffusion features providing crucial complementary information for challenging, ambiguous cases. DINO-v3 backbone significantly outperforms Swin-B (Table 7), demonstrating foundation model value. Three mask predictions also yield best performance, proving multi-mask effectiveness. Iterative generation Table 5 consistently improves performance with 3.6% F-measure gain on DIS datasets and 5.3% on DUT-OMRON, confirming the effectiveness of prioritizing challenging categories. LLM-generated prompts improve synthetic image quality with 44.7% Inception Score Table 8 increase over simple class names, highlighting prompt engineering importance.

## 6 CONCLUSION

We demonstrate that combining features from generative and discriminative models: diffusion feature maps, concept attention maps, and DINO-v3 representations enables effective synthetic data generation for salient object detection. Our iterative generation framework dynamically prioritizes challenging categories, while the ambiguity-aware architecture naturally handles multiple valid interpretations. This pipeline significantly improves cross-dataset generalization and provides a scalable framework for addressing data scarcity in dense prediction tasks, suggesting that synthetic data can effectively complement manual annotation in computer vision applications.

Table 7: **Architecture Ablation:** Multi-mask decoder improves performance on DIS-5K.

Backbone	$N_M$	$F_m \uparrow$	$S_\alpha \uparrow$	MAE $\downarrow$
Swin-B	1	.884	.883	.044
DINO-v3	1	.909	.911	.033
DINO-v3	2	.892	.896	.034
DINO-v3	3	<b>.914</b>	<b>.913</b>	<b>.031</b>

Table 8: **Prompt Generator:** LLM prompts improve diversity and quality.

Model	Prompt	CLIP $\uparrow$	IS $\uparrow$
S3OD	Class Name	.399	67.8
S3OD	GPT	<b>.434</b>	<b>.98.1</b>

---

## ACKNOWLEDGMENTS

This research was supported by the AIST policy-based budget project "R&D on Generative AI Foundation Models for the Physical Domain". Computational resources were provided by ABCI 3.0 from AIST and AIST Solutions. We are grateful to Andrew Zisserman for valuable discussions and feedback that helped improve this work.

## REFERENCES

- Radhakrishna Achanta, Sheila Hemami, Francisco Estrada, and Sabine Susstrunk. Frequency-tuned salient region detection. In *2009 IEEE conference on computer vision and pattern recognition*, pp. 1597–1604. IEEE, 2009.
- Josh Achiam, Steven Adler, Sandhini Agarwal, Lama Ahmad, Ilge Akkaya, Florencia Leoni Aleman, Diogo Almeida, Janko Altschmidt, Sam Altman, Shyamal Anadkat, et al. Gpt-4 technical report. *arXiv preprint arXiv:2303.08774*, 2023.
- Shekoofeh Azizi, Simon Kornblith, Chitwan Saharia, Mohammad Norouzi, and David J Fleet. Synthetic data from diffusion models improves imagenet classification. *arXiv preprint arXiv:2304.08466*, 2023.
- Black Forest Labs. Flux.1 [krea-dev]: Photorealistic image generation with enhanced realism. <https://bfl.ai/blog/flux-1-krea-dev>, 2025.
- Ali Borji, Ming-Ming Cheng, Huaizu Jiang, and Jia Li. Salient object detection: A benchmark. *IEEE transactions on image processing*, 24(12):5706–5722, 2015.
- Darren M Chan and Laurel D Riek. Unseen salient object discovery for monocular robot vision. *IEEE Robotics and Automation Letters*, 5(2):1484–1491, 2020.
- Alexey Dosovitskiy, Lucas Beyer, Alexander Kolesnikov, Dirk Weissenborn, Xiaohua Zhai, Thomas Unterthiner, Mostafa Dehghani, Matthias Minderer, Georg Heigold, Sylvain Gelly, et al. An image is worth 16x16 words: Transformers for image recognition at scale. *arXiv preprint arXiv:2010.11929*, 2020.
- Deng-Ping Fan, Ming-Ming Cheng, Yun Liu, Tao Li, and Ali Borji. Structure-measure: A new way to evaluate foreground maps. In *Proceedings of the IEEE international conference on computer vision*, pp. 4548–4557, 2017.
- Deng-Ping Fan, Cheng Gong, Yang Cao, Bo Ren, Ming-Ming Cheng, and Ali Borji. Enhanced-alignment measure for binary foreground map evaluation. *arXiv preprint arXiv:1805.10421*, 2018.
- Lijie Fan, Kaifeng Chen, Dilip Krishnan, Dina Katabi, Phillip Isola, and Yonglong Tian. Scaling laws of synthetic images for model training... for now. In *Proceedings of the IEEE/CVF Conference on Computer Vision and Pattern Recognition*, pp. 7382–7392, 2024.
- Mengyang Feng, Huchuan Lu, and Errui Ding. Attentive feedback network for boundary-aware salient object detection. In *Proceedings of the IEEE/CVF conference on computer vision and pattern recognition*, pp. 1623–1632, 2019.
- Stas Goferman, Lih Zelnik-Manor, and Ayellet Tal. Context-aware saliency detection. *IEEE transactions on pattern analysis and machine intelligence*, 34(10):1915–1926, 2011.
- Abner Guzman-Rivera, Dhruv Batra, and Pushmeet Kohli. Multiple choice learning: Learning to produce multiple structured outputs. *Advances in neural information processing systems*, 25, 2012.
- Kaiming He, Xiangyu Zhang, Shaoqing Ren, and Jian Sun. Deep residual learning for image recognition. In *Proceedings of the IEEE conference on computer vision and pattern recognition*, pp. 770–778, 2016.
- Alec Helbling, Tuna Han Salih Meral, Ben Hoover, Pinar Yanardag, and Duen Horng Chau. Conceptattention: Diffusion transformers learn highly interpretable features, 2025. URL <https://arxiv.org/abs/2502.04320>.

- 
- Laurynas Karazija, Iro Laina, Andrea Vedaldi, and Christian Rupprecht. Diffusion models for open-vocabulary segmentation. In *European Conference on Computer Vision*, pp. 299–317. Springer, 2024.
- Lei Ke, Mingqiao Ye, Martin Danelljan, Yu-Wing Tai, Chi-Keung Tang, Fisher Yu, et al. Segment anything in high quality. *Advances in Neural Information Processing Systems*, 36:29914–29934, 2023.
- Taehun Kim, Kunhee Kim, Joonyeong Lee, Dongmin Cha, Jiho Lee, and Daijin Kim. Revisiting image pyramid structure for high resolution salient object detection. In *Proceedings of the Asian Conference on Computer Vision*, pp. 108–124, 2022.
- Orest Kupyn and Christian Rupprecht. Dataset enhancement with instance-level augmentations. In *European Conference on Computer Vision*, pp. 384–402. Springer, 2024.
- Orest Kupyn, Eugene Khvedchenia, and Christian Rupprecht. Vggheads: A large-scale synthetic dataset for 3d human heads. *arXiv preprint arXiv:2407.18245*, 2024.
- Black Forest Labs. Flux. <https://github.com/black-forest-labs/flux>, 2023. URL <https://github.com/black-forest-labs/flux>.
- Tsung-Yi Lin, Priya Goyal, Ross Girshick, Kaiming He, and Piotr Dollár. Focal loss for dense object detection. In *Proceedings of the IEEE international conference on computer vision*, pp. 2980–2988, 2017.
- Feng Liu, Luan Tran, and Xiaoming Liu. Fully understanding generic objects: Modeling, segmentation, and reconstruction. In *Proceedings of the IEEE/CVF Conference on Computer Vision and Pattern Recognition*, pp. 7423–7433, 2021a.
- Ze Liu, Yutong Lin, Yue Cao, Han Hu, Yixuan Wei, Zheng Zhang, Stephen Lin, and Baining Guo. Swin transformer: Hierarchical vision transformer using shifted windows. In *Proceedings of the IEEE/CVF international conference on computer vision*, pp. 10012–10022, 2021b.
- Federico Perazzi, Philipp Krähenbühl, Yael Pritch, and Alexander Hornung. Saliency filters: Contrast based filtering for salient region detection. In *2012 IEEE conference on computer vision and pattern recognition*, pp. 733–740. IEEE, 2012.
- Jordi Pont-Tuset, Federico Perazzi, Sergi Caelles, Pablo Arbeláez, Alex Sorkine-Hornung, and Luc Van Gool. The 2017 davis challenge on video object segmentation. *arXiv preprint arXiv:1704.00675*, 2017.
- Haotian Qian, Yinda Chen, Shengtao Lou, Fahad Khan, Xiaogang Jin, and Deng-Ping Fan. Maskfactory: Towards high-quality synthetic data generation for dichotomous image segmentation. In *The Thirty-eighth Annual Conference on Neural Information Processing Systems*, 2024.
- Xuebin Qin, Zichen Zhang, Chenyang Huang, Chao Gao, Masood Dehghan, and Martin Jagersand. Basnet: Boundary-aware salient object detection. In *Proceedings of the IEEE/CVF conference on computer vision and pattern recognition*, pp. 7479–7489, 2019.
- Xuebin Qin, Zichen Zhang, Chenyang Huang, Masood Dehghan, Osmar R Zaiane, and Martin Jagersand. U2-net: Going deeper with nested u-structure for salient object detection. *Pattern recognition*, 106:107404, 2020.
- Xuebin Qin, Hang Dai, Xiaobin Hu, Deng-Ping Fan, Ling Shao, and Luc Van Gool. Highly accurate dichotomous image segmentation. In *European Conference on Computer Vision*, pp. 38–56. Springer, 2022.
- René Ranftl, Alexey Bochkovskiy, and Vladlen Koltun. Vision transformers for dense prediction. In *Proceedings of the IEEE/CVF international conference on computer vision*, pp. 12179–12188, 2021.
- Nikhila Ravi, Valentin Gabeur, Yuan-Ting Hu, Ronghang Hu, Chaitanya Ryali, Tengyu Ma, Haitham Khedr, Roman Rädle, Chloe Rolland, Laura Gustafson, et al. Sam 2: Segment anything in images and videos. *arXiv preprint arXiv:2408.00714*, 2024.

- 
- Robin Rombach, Andreas Blattmann, Dominik Lorenz, Patrick Esser, and Björn Ommer. High-resolution image synthesis with latent diffusion models. In *Proceedings of the IEEE/CVF conference on computer vision and pattern recognition*, pp. 10684–10695, 2022.
- Christian Rupprecht, Iro Laina, Robert DiPietro, Maximilian Baust, Federico Tombari, Nassir Navab, and Gregory D Hager. Learning in an uncertain world: Representing ambiguity through multiple hypotheses. In *Proceedings of the IEEE international conference on computer vision*, pp. 3591–3600, 2017.
- Mert Bülent Saryıldız, Karteek Alahari, Diane Larlus, and Yannis Kalantidis. Fake it till you make it: Learning transferable representations from synthetic imagenet clones. In *Proceedings of the IEEE/CVF Conference on Computer Vision and Pattern Recognition*, pp. 8011–8021, 2023.
- Christoph Schuhmann, Romain Beaumont, Richard Vencu, Cade Gordon, Ross Wightman, Mehdi Cherti, Theo Coombes, Aarush Katta, Clayton Mullis, Mitchell Wortsman, et al. Laion-5b: An open large-scale dataset for training next generation image-text models. *Advances in neural information processing systems*, 35:25278–25294, 2022.
- Jordan Shipard, Arnold Wiliem, Kien Nguyen Thanh, Wei Xiang, and Clinton Fookes. Diversity is definitely needed: Improving model-agnostic zero-shot classification via stable diffusion. In *Proceedings of the IEEE/CVF Conference on Computer Vision and Pattern Recognition*, pp. 769–778, 2023.
- Oriane Siméoni, Huy V Vo, Maximilian Seitzer, Federico Baldassarre, Maxime Oquab, Cijo Jose, Vasil Khalidov, Marc Szafraniec, Seungeun Yi, Michaël Ramamonjisoa, et al. Dinov3. *arXiv preprint arXiv:2508.10104*, 2025.
- Gemma Team, Aishwarya Kamath, Johan Ferret, Shreya Pathak, Nino Vieillard, Ramona Merhej, Sarah Perrin, Tatiana Matejovicova, Alexandre Ramé, Morgane Rivière, et al. Gemma 3 technical report. *arXiv preprint arXiv:2503.19786*, 2025.
- Yang Tian, Hualong Bai, Shengdong Zhao, Chi-Wing Fu, Chun Yu, Haozhao Qin, Qiong Wang, and Pheng-Ann Heng. Kine-appendage: Enhancing freehand vr interaction through transformations of virtual appendages. *IEEE Transactions on Visualization and Computer Graphics*, 2022.
- Yonglong Tian, Lijie Fan, Phillip Isola, Huiwen Chang, and Dilip Krishnan. Stablerep: Synthetic images from text-to-image models make strong visual representation learners. *arXiv preprint arXiv:2306.00984*, 2023.
- Ashish Vaswani, Noam Shazeer, Niki Parmar, Jakob Uszkoreit, Llion Jones, Aidan N Gomez, Łukasz Kaiser, and Illia Polosukhin. Attention is all you need. *Advances in neural information processing systems*, 30, 2017.
- Lijun Wang, Huchuan Lu, Yifan Wang, Mengyang Feng, Dong Wang, Baocai Yin, and Xiang Ruan. Learning to detect salient objects with image-level supervision. In *Proceedings of the IEEE conference on computer vision and pattern recognition*, pp. 136–145, 2017.
- Wenguan Wang, Shuyang Zhao, Jianbing Shen, Steven CH Hoi, and Ali Borji. Salient object detection with pyramid attention and salient edges. In *Proceedings of the IEEE/CVF conference on computer vision and pattern recognition*, pp. 1448–1457, 2019.
- Jun Wei, Shuhui Wang, Zhe Wu, Chi Su, Qingming Huang, and Qi Tian. Label decoupling framework for salient object detection. In *Proceedings of the IEEE/CVF conference on computer vision and pattern recognition*, pp. 13025–13034, 2020.
- Weijia Wu, Yuzhong Zhao, Hao Chen, Yuchao Gu, Rui Zhao, Yefei He, Hong Zhou, Mike Zheng Shou, and Chunhua Shen. Datasetdm: Synthesizing data with perception annotations using diffusion models. *arXiv preprint arXiv:2308.06160*, 2023a.
- Weijia Wu, Yuzhong Zhao, Mike Zheng Shou, Hong Zhou, and Chunhua Shen. Diffumask: Synthesizing images with pixel-level annotations for semantic segmentation using diffusion models. *arXiv preprint arXiv:2303.11681*, 2023b.

- 
- Zhe Wu, Li Su, and Qingming Huang. Cascaded partial decoder for fast and accurate salient object detection. In *Proceedings of the IEEE/CVF conference on computer vision and pattern recognition*, pp. 3907–3916, 2019a.
- Zhe Wu, Li Su, and Qingming Huang. Stacked cross refinement network for edge-aware salient object detection. In *Proceedings of the IEEE/CVF international conference on computer vision*, pp. 7264–7273, 2019b.
- Zhenyu Wu, Lin Wang, Wei Wang, Tengfei Shi, Chenglizhao Chen, Aimin Hao, and Shuo Li. Synthetic data supervised salient object detection. In *Proceedings of the 30th ACM International Conference on Multimedia*, pp. 5557–5565, 2022.
- Chenxi Xie, Changqun Xia, Mingcan Ma, Zhirui Zhao, Xiaowu Chen, and Jia Li. Pyramid grafting network for one-stage high resolution saliency detection. In *Proceedings of the IEEE/CVF conference on computer vision and pattern recognition*, pp. 11717–11726, 2022.
- Chuan Yang, Lihe Zhang, Huchuan Lu, Xiang Ruan, and Ming-Hsuan Yang. Saliency detection via graph-based manifold ranking. In *Proceedings of the IEEE conference on computer vision and pattern recognition*, pp. 3166–3173, 2013.
- Ryota Yoshihashi, Yuya Otsuka, Tomohiro Tanaka, Hirokatsu Kataoka, et al. Exploring limits of diffusion-synthetic training with weakly supervised semantic segmentation. In *Proceedings of the Asian Conference on Computer Vision*, pp. 2300–2318, 2024.
- Qian Yu, Xiaoqi Zhao, Youwei Pang, Lihe Zhang, and Huchuan Lu. Multi-view aggregation network for dichotomous image segmentation. In *Proceedings of the IEEE/CVF Conference on Computer Vision and Pattern Recognition*, pp. 3921–3930, 2024.
- Yi Zeng, Pingping Zhang, Jianming Zhang, Zhe Lin, and Huchuan Lu. Towards high-resolution salient object detection. In *Proceedings of the IEEE/CVF international conference on computer vision*, pp. 7234–7243, 2019.
- Xiaoning Zhang, Tiantian Wang, Jinqing Qi, Huchuan Lu, and Gang Wang. Progressive attention guided recurrent network for salient object detection. In *Proceedings of the IEEE conference on computer vision and pattern recognition*, pp. 714–722, 2018.
- Jia-Xing Zhao, Jiang-Jiang Liu, Deng-Ping Fan, Yang Cao, Jufeng Yang, and Ming-Ming Cheng. Egnet: Edge guidance network for salient object detection. In *Proceedings of the IEEE/CVF international conference on computer vision*, pp. 8779–8788, 2019.
- Peng Zheng, Dehong Gao, Deng-Ping Fan, Li Liu, Jorma Laaksonen, Wanli Ouyang, and Nicu Sebe. Bilateral reference for high-resolution dichotomous image segmentation. *arXiv preprint arXiv:2401.03407*, 2024.

---

## A PROMPTING

To further enhance the quality and diversity of our synthetic data, we employed an LLM Achiam et al. (2023) to generate detailed, specific prompts rather than using simple class names. The prompting strategy was designed to systematically vary key aspects of scene composition including object size, positioning, occlusion levels, lighting conditions, and environmental complexity. For example, when generating "lion" category images, prompts varied from scenes with multiple lions to single lions in challenging environmental conditions. These detailed textual descriptions guided the diffusion model to create more challenging, diverse training samples that better reflect real-world scenarios and edge cases. The set of example prompts for the "lion" category includes:

1. A medium-sized lion lying on a sunlit rock, partially obscured by tall grass, with a dense forest background; intricate shadows play on the lion's fur and the rock surface.
2. A small lion cub, occupying the left third of the frame, peeking through a thicket of dry branches in a savannah setting with blurred golden grass and a distant treeline.
3. Two lions resting under the shade of an acacia tree, one lion partially hidden by the tree's trunk; dappled sunlight filters through the leaves, creating complex patterns on the ground.
4. A majestic lion standing on a hilltop, backlit by the setting sun, casting a dramatic silhouette against a vibrant, cloud-streaked sky with the savannah stretching out in the background.
5. A close-up of a lion's face, centered in the frame, with its mane blending into a similarly colored rocky background; fine textures of the fur and rock are sharply defined.
6. A trio of lions walking through a misty grassland, with their figures partly obscured by the fog; subtle variations in coloration and mane distinguish each lion.
7. A lioness crouching low in a field of tall yellow grass, partially obscured and camouflaged by the foliage, with a clear blue sky above and distant hills in the background.
8. A large male lion resting near a waterhole, with its reflection visible in the water; surrounding reeds and scattered stones add complexity to the scene.
9. A lion moving through a snowy landscape, with snowflakes gently falling; the lion's fur stands out against the whiteness, and scattered bushes break the monotony of the snow.
10. A wide shot of a lion pride relaxing in the shade of a large rock formation, with varied poses and partial occlusions by rocks; the background features a lush green valley.

The full system prompt is presented in fig. 5

## B DATASET QUALITY

We conducted a quality assessment of our synthetic dataset across multiple dimensions. Manual verification of 1,000 randomly sampled masks revealed high annotation quality: only 14 samples (1.4%) exhibited minor issues such as slightly incomplete mask boundaries, while merely 1 sample (0.1%) was missing a clear foreground object entirely. This demonstrates the effectiveness of our multi-stage filtering pipeline and multi-modal dataset diffusion approach.

Another significant challenge in synthetic data generation is the domain gap between synthetic and real images. We observed that standard FLUX model fine-tuned for aesthetics produce unnaturally oversaturated images that differ substantially from real-world photography. To address this, we employ the FLUX-Krea checkpoint Black Forest Labs (2025), which underwent large-scale reinforcement learning alignment specifically for photorealism, producing significantly more natural-looking images. Additionally, during pretraining we apply comprehensive image augmentations to further reduce the synthetic-to-real domain gap.

We evaluate synthetic data quality using standard generative model metrics compared to existing approaches. As shown in Table 9, our method achieves superior image quality and diversity comparing to datasets based on older diffusion models. S3OD achieves an Inception Score of 35.19 compared to MaskFactory's 17.41 and DatasetDM's 14.97, indicating better diversity and quality. Our FID score of 1.74 significantly outperforms MaskFactory (2.81) and DatasetDM (3.16), demonstrating closer similarity to real data distribution.

System Prompt for Salient Object Detection Data Generation			
Generate exactly {num_prompts} diverse prompts for {main_class} images for salient object detection. Focus on natural, photorealistic scenes with varying complexity.			
Focus on natural, photorealistic scenes with an elevated level of realism, complexity, and diversity.			
<b>Key aspects to vary:</b>			
<ul style="list-style-type: none"> <li>• <b>Object size:</b> Include scenes with small main objects (occupying 10-30% of the frame) as well as larger instances, ensuring varied prominence.</li> <li>• <b>Object position:</b> Vary placement between center, left, and right sides of the frame.</li> <li>• <b>Multiple instances:</b> Occasionally include 2-3 distinct instances of the main object, each with subtle differences in appearance or partial occlusion.</li> <li>• <b>Visual complexity:</b> Integrate rich textures, intricate patterns, and similarly-colored natural background elements that challenge segmentation.</li> <li>• <b>Occlusion:</b> Introduce partial occlusion by natural elements (10-20% occlusion) to add depth.</li> <li>• <b>Lighting:</b> Vary between harsh shadows, dramatic backlighting, and dappled sunlight, ensuring that all lighting conditions remain natural.</li> <li>• <b>Environment:</b> Use visually busy natural settings with detailed foreground, midground, and background elements that contribute to overall scene complexity. Include challenging conditions such as fog, rain, snow, or dusty haze to heighten realism if appropriate.</li> <li>• <b>Viewpoint:</b> Mix close-ups, medium shots, and wide perspectives for diverse scene compositions.</li> <li>• <b>Additional elements:</b> Ensure the main object remains identifiable in the foreground, integrated into a naturally complex setting without relying on artificial or softened effects.</li> </ul>			
<b>Essential requirements:</b>			
<ul style="list-style-type: none"> <li>• The main object(s) must be clearly discernible for salient object detection, yet embedded within a challenging, detailed environment.</li> <li>• Avoid artificial or studio setups—use only natural settings and lighting.</li> <li>• Maintain sharp focus across all scene elements to ensure realism; do not include any blur, bokeh, or artificially softened backgrounds.</li> <li>• The background should be naturally complex and detailed, providing a challenging context for segmentation without compromising the visibility of the main object.</li> </ul>			
Return exactly {num_prompts} prompts as Python list: ["A description of a scene", ...]			
Important: Double-check that your response contains exactly {num_prompts} prompts.			

Figure 5: The complete system prompt used to instruct the LLM Achiam et al. (2023) for generating diverse text descriptions. These descriptions focus on creating natural scenes with varying complexity, occlusion, and lighting to simulate challenging real-world conditions for salient object detection.

Table 9: **Dataset Quality Comparison:** S3OD generated with large DiT model fine-tuned for photorealism achieves substantially higher quality and better real-data alignment compared to existing synthetic approaches, demonstrating the importance of realistic generation models.

Method	Diffusion Model	Inception Score ↑	FID ↓
S3OD	FLUX-Krea Black Forest Labs (2025)	<b>35.19</b>	<b>1.74</b>
S3OD	FLUX-dev Labs (2023)	31.94	1.90
MaskFactory	Stable Diffusion Rombach et al. (2022)	17.41	2.81
DatasetDM	Stable Diffusion Rombach et al. (2022)	14.97	3.16

## C QUALITATIVE EVALUATION

We visualize the random samples from different categories of S3OD in fig. 6. It demonstrate the diversity and realism achieved by our synthetic data generation pipeline, spanning various object types, lighting conditions, and scene compositions. The samples exhibit challenging scenarios with complex backgrounds, partial occlusions, and varying object: key attributes for training robust salient

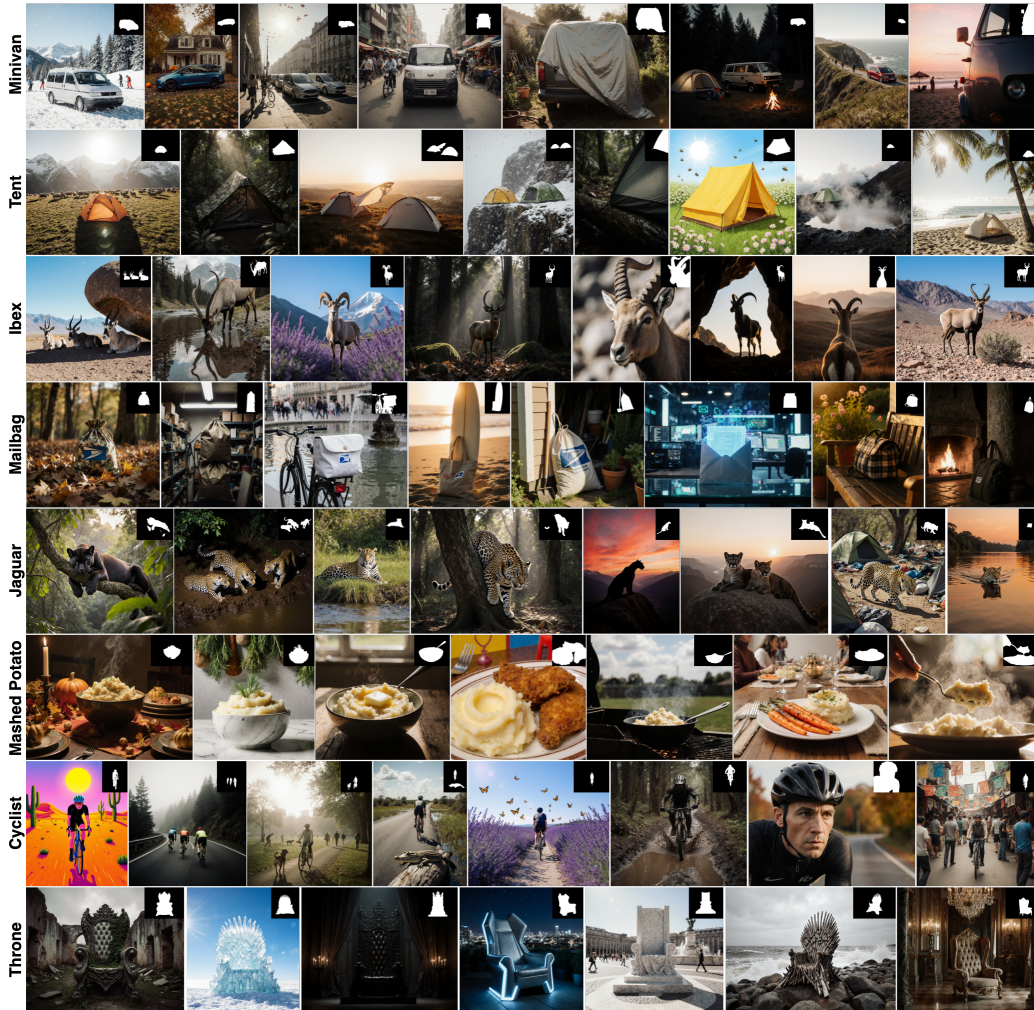


Figure 6: **S3OD Dataset Samples:** Our method generates diverse high quality samples across a wide variety of object categories.

object detection models. As shown in Figure 7, LLM-based prompt generation significantly enhances the visual quality and diversity.

## D MODEL DETAILS

Our model achieves a strong balance between performance and efficiency as shown in Table 10, comparable to other state-of-the-art models that utilize large transformer backbones. Notably, the model is both more efficient and has more parameters comparing to models that are based on the Swin architecture Liu et al. (2021b). The DINO-v3 Siméoni et al. (2025) backbone with ViT-B Dosovitskiy et al. (2020) offers a favorable trade-off between computational efficiency and state-of-the-art performance.

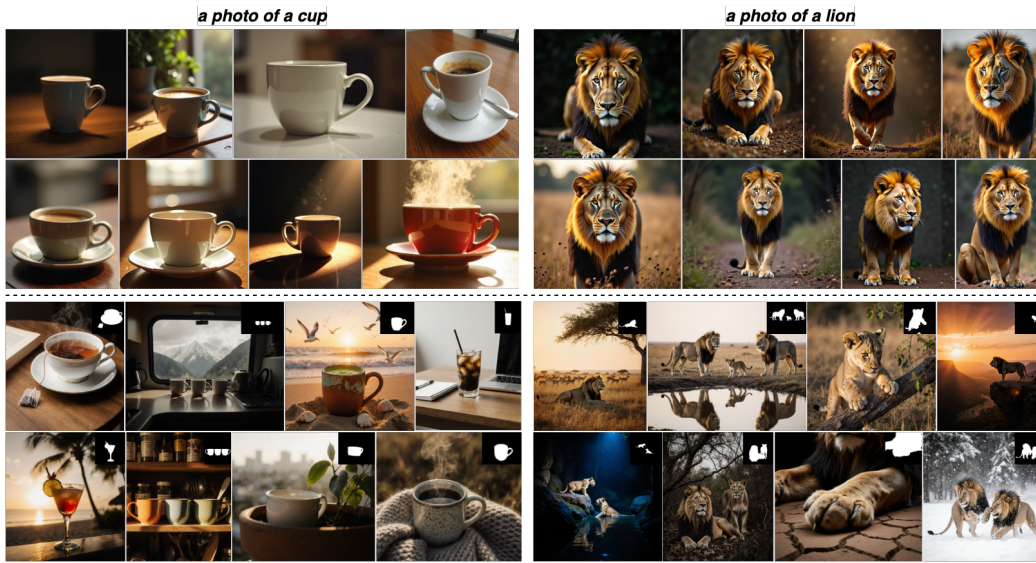


Figure 7: **Prompt Enhancement**: Top: Class name as a prompt. Bottom: LLM Prompt Generator. By focusing on key properties of salient object detection dataset the agent creates detailed and diverse prompts to maximize the diversity and realism.

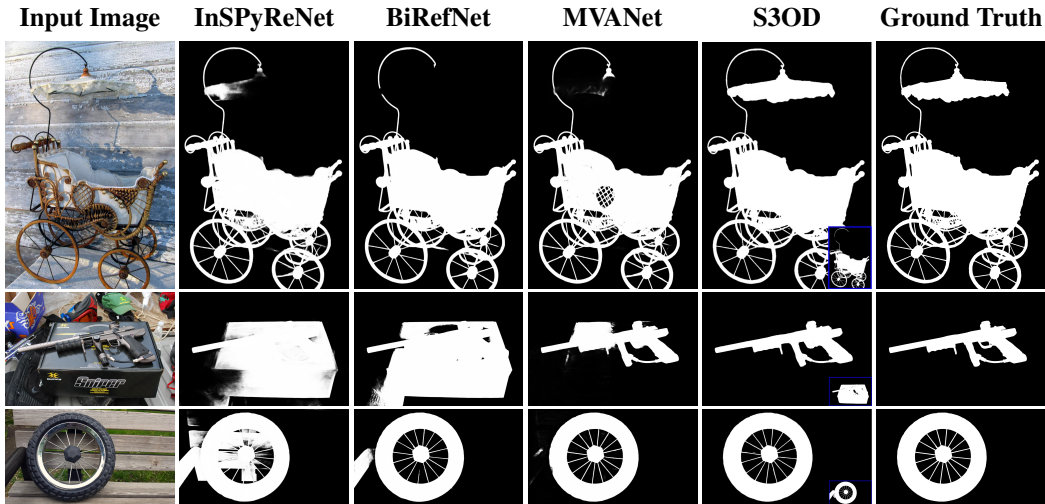


Figure 8: Qualitative comparison vs state-of-the-art methods on DIS-5K Qin et al. (2022) dataset. By modeling multiple hypothesis S3OD is able to predict detailed masks with high confidence. Alternative prediction can be seen in the bottom right corner.

Table 10: **Model Efficiency**. S3OD achieves comparable performance to other state-of-the-art salient object detection methods.

Model	Total Parameters	FLOPs (T)	FPS
InSPyReNet Kim et al. (2022)	90,721,443	1.495	2.88
BiRefNet Zheng et al. (2024)	220,176,498	1.143	3.65
MVANet Yu et al. (2024)	94,139,021	0.857	4.62
S3OD	116,905,286	0.807	3.80